Journal of Materials Chemistry C

ROYAL SOCIETY OF CHEMISTRY

PAPER

View Article Online
View Journal

Cite this: DOI: 10.1039/d5tc04503g

Superior energy storage performance of $PbZrO_3$-based films *via* phase regulation and entropy engineering

Jiaqi Lian,[a] Fengzhen Huang, *[ab] Biwei Shen,[a] Yulong Yang,[a] Jielin Zha,[a] Zeyu Xiao,[a] Kai Cao,[a] Xiaomei Lu *[ab] and Jinsong Zhu[ab]

Achieving a synchronous improvement of recoverable energy storage density (W_{rec}) and efficiency (η) remains a critical challenge for dielectric capacitors. In this paper, a synergistic strategy combining phase regulation and entropy engineering is proposed to delay the transition from the antiferroelectric (AFE) to ferroelectric (FE) phase and enhance the relaxor behavior of the $PbZrO_3$ (PZO) film, optimizing both W_{rec} and η. Specifically, Sn^{4+} at the B site induces a tetragonal AFE phase within the orthorhombic AFE matrix of PZO, which reduces the domain size and facilitates the FE–AFE polarization switching upon removal of the applied electric field. La^{3+}, Sr^{2+}, and Ba^{2+} at the A site stabilize the AFE phase by reducing the perovskite tolerance factor and thus increase the transition field from the AFE to FE phase. Furthermore, the high-entropy design refines the microstructure and stabilizes the charge carriers through introducing chemical disorder, effectively reducing the leakage current and enhancing the breakdown field. Consequently, a large W_{rec} of 101.8 J cm^{-3} and an η of 71.5% are achieved in the $Pb_{0.895}La_{0.03}Sr_{0.03}Ba_{0.03}Zr_{0.5}Sn_{0.5}O_3$ relaxor AFE thin film, approximately 3.6- and 2-fold higher than those of pure PZO, respectively. This relaxor AFE film also exhibits excellent breakdown reliability, superior thermal stability and robust fatigue resistance.

Received 25th December 2025,
Accepted 6th February 2026

DOI: 10.1039/d5tc04503g

rsc.li/materials-c

1. Introduction

Compared with electrochemical capacitors, dielectric capacitors based on physical polarization offer ultrahigh power density, rapid charge–discharge rates, and exceptional stability, making them suitable for high-power pulse systems, military defense and microwave communications.[1–3] However, the low energy density and efficiency limit their use in compact devices. Therefore, developing advanced dielectric materials that can simultaneously achieve high energy density and efficiency has become a focus of ongoing research. The energy storage performance of dielectric capacitors is determined mainly by polarization (P) switching under an applied electric field (E), with the key parameters obtained from the P–E loops using the following equations:[4]

$$W = \int_0^{P_m} E\mathrm{d}P \quad (1)$$

$$W_{rec} = \int_{P_r}^{P_m} E\mathrm{d}P \quad (2)$$

$$\eta = \frac{W_{rec}}{W} \times 100\% \quad (3)$$

where W, W_{rec}, P_m, P_r, and η represent the total energy storage density, recoverable energy density, maximum polarization, remnant polarization, and efficiency, respectively. It is seen that a large polarization difference ($\Delta P = P_m - P_r$) and a high breakdown field (E_b) are pivotal for good energy storage performance, while a trade-off between them is commonly observed for conventional linear dielectrics (LDs) and ferroelectrics (FEs).[5] Antiferroelectrics (AFEs), benefiting from the field-induced reversible AFE–FE transition, exhibit distinctive double hysteresis loops, where AFEs transform into FEs under the forward switching field (E_F), and revert to AFEs under the backward switching field (E_A) (Fig. S1). The antiparallel alignment of polarization results in a near-zero P_r, making AFEs promising candidates for energy storage.[6]

As a typical AFE material, $PbZrO_3$ (PZO) has drawn extensive interest in dielectric energy storage due to its high polarization and flexible compositional tunability. However, the small free energy difference between AFE and FE phases makes its AFE order highly sensitive to external perturbations, resulting in a

[a] National Laboratory of Solid State Microstructures and Physics School, Nanjing University, Nanjing, 210093, China. E-mail: fzhuang@nju.edu.cn, xiaomeil@nju.edu.cn
[b] Collaborative Innovation Center of Advanced Microstructures, Nanjing University, Nanjing, 210093, China

non-zero P_r and a low η (<50%).[7,8] Furthermore, the lattice distortion accompanying the AFE–FE transition under an electric field leads to fast polarization saturation and low dielectric breakdown strength, limiting both W_{rec} and η. To stabilize the AFE phase of PZO, various strategies were explored, including grain refinement,[9,10] chemical doping,[11–20] oriented growth,[21–23] and defect engineering.[24] For example, Li *et al.* achieved a W_{rec} of 31 J cm^{-3} and an η of 65% through grain refinement,[10] and later improved W_{rec} and η to 50 J cm^{-3} and 78%, respectively, by co-doping La^{3+} and Sr^{2+} at the A site.[11] To enhance the relaxor behavior of AFE–FE transition, strategies such as entropy engineering,[25–27] solid-solution design[28,29] and interfacial optimization[30–33] were developed. Shen *et al.* designed PZO-$SrTiO_3$ relaxor ferroelectrics with multi-state nano-domains, enabling excellent energy storage performance (W_{rec} ~ 73.7 J cm^{-3} and η ~ 72%).[28] Son *et al.* demonstrated that high entropy $(Pb_{0.87}Sr_{0.05}Ba_{0.05}La_{0.02})(Zr_{0.52}Sn_{0.40}Ti_{0.08})O_3$ films exhibited low lattice mismatch during AFE–FE transition, yielding a large W_{rec} of 88 J cm^{-3} and an η of 85%.[34]

Although notable progress has been made in improving the W_{rec} and η of PZO, there are still two challenges. First, a FE state usually appears during phase regulation, losing a portion of W_{rec} prior to the AFE–FE transition. Second, the relaxation of the AFE–FE transition usually increases η but decreases P_{max}, resulting in the trade-off between W_{rec} and η. In this paper, a synergistic strategy combining phase regulation and entropy engineering is proposed to concurrently optimize W_{rec} and η of PZO. As shown in Fig. 1, incorporating Sn^{4+} at the B site can induce a tetragonal antiferroelectric (AFE_T) phase, an AFE phase similar to that in $PbSnO_3$ (PSO).[35] The coexistence of orthorhombic antiferroelectric (AFE_O) and AFE_T can not only facilitate polarization switching, leading to decreased P_r, but also enhance the relaxor behavior of AFE–FE transition and the lattice disorder, resulting in the delay of polarization saturation and the improvement of E_b. Given that the antiferroelectricity of PZO originates from the antiparallel polarization of Pb^{2+} ions and the antiphase tilting of $[ZrO_6]$ octahedra,[36] A-site doping is synchronously adopted to stabilize the AFE phase. The phase stability of ABO_3-type perovskites can be evaluated using the tolerance factor t:[37]

$$t = \frac{R_A + R_O}{\sqrt{2}(R_B + R_O)} \quad (4)$$

where R_A, R_B and R_O represent the ionic radii of A-site cations, B-site cations and oxygen anions, respectively. In general, $t > 1$ and $t < 1$, respectively, favor the FE and AFE phases. Accordingly, equal amounts of La^{3+}, Sr^{2+} and Ba^{2+} ions are introduced to reduce t and to acquire a higher atomic configurational entropy:[38]

$$S_{config} = -R\left[\left(\sum_{i=1}^{N} x_i \ln x_i\right)_{cation\text{-}site} + \left(\sum_{j=1}^{M} x_j \ln x_j\right)_{anion\text{-}site}\right] \quad (5)$$

where R is the gas constant, N/M are the numbers of cation/anion species, and x_i/x_j are the corresponding mole fractions.

Following these principles, a series of $Pb_{1-3.5x}La_xSr_xBa_xZr_{1-y}Sn_yO_3$ (abbreviated as x-PLSB/y-ZSO) films are prepared to obtain relaxor antiferroelectrics (RAFEs). It is found that Sn^{4+} at the B site transforms PZO from AFE_O to RAFE with the coexistence of AFE_O and AFE_T, and the incorporation of La^{3+}, Sr^{2+} and Ba^{2+} at the A site delays the field-induced AFE–FE transition and further enhances its relaxor behavior. This, along with the significantly enhanced E_b in the high-entropy $Pb_{0.895}La_{0.03}Sr_{0.03}Ba_{0.03}Zr_{0.5}Sn_{0.5}O_3$ film causes a simultaneous improvement in W_{rec} (~101.8 J cm^{-3}) and η (~71.5%), as well as excellent thermal and cycling stability.

2. Experimental details

PZO, x-PLSB/y-ZSO (x = 0.02 and 0.03; y = 0.4, 0.5, and 0.6) and x-PLSB/0.5-ZSO (x = 0, 0.02, 0.03, and 0.04) thin films were fabricated on Pt/Ti/SiO_2/Si substrates *via* a metal organic decomposition method. The preparation began with dissolving

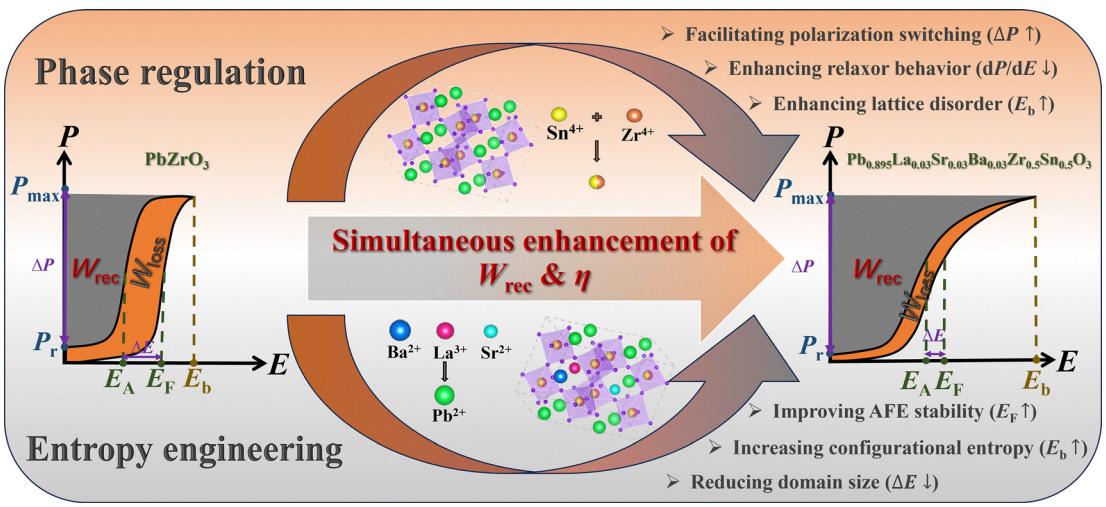

Fig. 1 Schematic diagram of the phase regulation and entropy engineering strategy.

$Pb(CH_3COO)_2{\cdot}3H_2O$ (99.5%), $La(NO_3)_3$-nH_2O (88%), $Sr(CH_3COO)_2$-$1/2H_2O$ (99%), $C_4H_6BaO_4$ (99%) and $C_8H_{12}O_8Sn$ (95%) in a mixed solvent of CH_3COOH (99.5%) and deionized water at a volume ratio of 9 : 1, and 10 mol% excess $Pb(CH_3COO)_2{\cdot}3H_2O$ was added to compensate for Pb volatilization during high-temperature annealing. Simultaneously, $C_{12}H_{28}O_4Zr$ (70%) was dissolved in $C_3H_8O_2$ (99.5%). The two solutions were stirred separately at room temperature for 2 h to ensure complete dissolution and then mixed. The resulting solution was adjusted to 0.2 M with $C_3H_8O_2$ and stirred for 6 h at room temperature to obtain a clear, transparent precursor solution. After aging for 72 h, the precursor solution was spin-coated on a Pt/Ti/SiO_2/Si substrate at 1000 rpm for 5 s, followed by 3500 rpm for 25 s to form a uniform film. The coated films were preheated on a 200 °C hot plate for 5 min to remove organic solvents. Subsequently, rapid thermal annealing (RTP-500) was performed in an oxygen atmosphere, heating to 700 °C at a rate of 30 °C s^{-1}, holding for 8 min and allowing natural cooling to room temperature. The spin-coating and annealing steps were repeated until the desired film thickness was achieved. Finally, the films were annealed in oxygen for 15 min. Prior to the electrical measurement, Pt dot electrodes with 0.2 mm in diameter were deposited on the film surface *via* sputtering.

Crystal structures were analyzed by X-ray diffraction (XRD, Bruker D8, Cu Kα radiation). The microstructure and morphology were characterized using scanning electron microscopy (SEM, Gemini 500) combined with energy dispersive spectroscopy (EDS), atomic force microscopy (AFM, Icon), piezoresponse force microscopy (PFM, Icon), high-resolution transmission electron microscopy (HR-TEM, FEI Tecnai G2 F30) and aberration-corrected high-angle annular dark-field scanning transmission electron microscopy (AC HAADF-STEM, Cubed Themis G2 300). The chemical states of O 1s were analyzed by X-ray photoelectron spectroscopy (XPS, Thermo Scientific Nexsa G2). Electrical measurements, including ferroelectric hysteresis, leakage current and dielectric spectra, were measured using a standard FE test system (Precision Multiferroic, Radiant Technologies) at 1 kHz and an impedance analyzer (HP4194A) equipped with a heating/cooling stage (TMS94) under 0.5 V AC, over 0.1–100 kHz. For leakage current measurements, a delay time of 1 s was applied at each voltage step to ensure measurement stability.

3. Results and discussion

3.1. Crystal structure and microstructure

Since both A-site and B-site ion doping influence the energy storage performance of PZO, we first investigate the impact of the Zr^{4+}/Sn^{4+} ratio at the B site to simplify the mechanism analysis. Detailed discussion of *P*–*E* loops, XRD patterns and temperature-dependent dielectric spectra are given in Fig. S2–S4. The results show that the energy storage performance is optimal when the Zr^{4+}/Sn^{4+} ratio is 1 : 1 (y = 0.5). In the following, we prepare a series of films with a fixed B-site component (y = 0.5) while different A-site components, x-PLSB/0.5-ZSO (x = 0, 0.02, 0.03, and 0.04), and systematically investigate their structural, electrical and energy storage characteristics. Meanwhile, the corresponding results of pure PZO are also provided for a comparison.

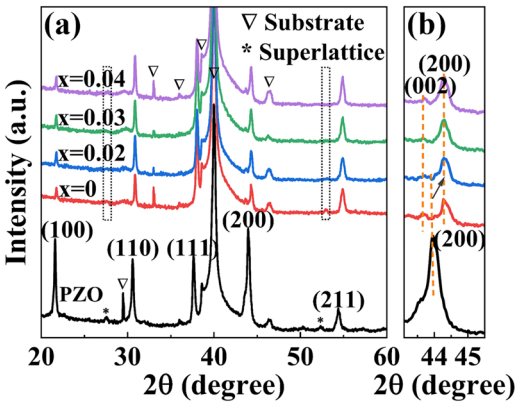

Fig. 2 (a) RT XRD patterns of PZO and x-PLSB/0.5-ZSO films, and (b) the magnified view around the (200) diffraction peak.

Fig. 2(a) shows the room-temperature (RT) XRD patterns of PZO and x-PLSB/0.5-ZSO thin films, with all diffraction peaks indexed to a pseudocubic structure. All the films possess a single-phase perovskite structure. Fig. 2(b) presents a magnified view around the (200) diffraction peak. Compared with PZO, the incorporation of smaller-radius Sn^{4+} at the B site significantly shifts the (200) peak toward higher angles, and the emergence of the (002) peak suggests the appearance of the AFE_T phase. For the subsequent A-site doping, with increasing x, though the (200) peak shows only a slight shift toward higher angles, the superlattice diffraction peaks (marked with * in Fig. 2(a)), which originate from the $a^{--}c^0$-type antiphase tilting of oxygen octahedra in PZO,[39] gradually weaken and become indistinguishable, indicating the disruption of long-range AFE order. The uniform EDS mapping (Fig. S5) further confirms that the doping ions enter the perovskite structure and randomly distribute across the films.

Fig. S6 and S7 present the cross-sectional SEM images and surface AFM morphologies of the PZO and x-PLSB/0.5-ZSO films. The average film thickness is approximately 260 nm for all the films. As shown in Fig. S7, compared to the PZO film with a uniform grain size of about 20 nm, the average grain size of x-PLSB/0.5-ZSO films monotonically decreases while the size inhomogeneity first increases and then decreases due to the competition of AFE_O and AFE_T phases during the nucleation and growth process. As a result, a denser microstructure is obtained in the 0.03-PLSB/0.5-ZSO film, with small nanograins filling the spaces among larger grains, which is crucial for dielectric energy storage.[40] Although a smaller average grain size (~15 nm) is observed in the 0.04-PLSB/0.5-ZSO film, its relatively uniform size distribution leads to reduced compactness, similar to that of the PZO film.

3.2. Dielectric and energy storage properties

Fig. 3(a)–(e) show the temperature-dependent dielectric constant (ε_r) and loss (tanδ) of PZO and x-PLSB/0.5-ZSO films, with

the temperature ranging from 30 to 300 °C, covering all the phase transition temperatures of the samples. Four features are noteworthy. First, as shown in Fig. 3(a), the pure PZO film exhibits a set of frequency-independent dielectric peaks around 267 °C, corresponding to the transition from the AFE_O phase to paraelectric phase. Second, these peaks become frequency-dependent broad peaks and shift toward RT (Fig. 3(b)) due to the introduction of Sn^{4+}. Third, with increasing x, the broadening of the frequency-dependent dielectric peaks becomes more evident (Fig. 3(b)–(e)), indicating the enhancement of relaxor behavior. The temperature-dependent ε_r measured at 10^5 Hz is analyzed after subtracting the leakage conduction background, which usually increases with increasing temperature and thus may shift the peak position toward higher temperature. As shown in the insets of Fig. 3(b)–(e), with the increase of x, the transition temperature slightly decreases while the full width at half maximum (FWHM) obviously increases. That is to say, though the introduction of La^{3+}, Sr^{2+} and Ba^{2+} at the A site exhibits a minimal influence on the phase transition temperature range, it induces a more pronounced relaxor phase transition. To quantify this effect, ε_r above T_m (peak temperature) is analyzed using the following equation:[41]

$$\frac{\varepsilon_{r,m}}{\varepsilon_r} = 1 + \frac{(T - T_m)^\gamma}{2\sigma^2} \quad (6)$$

where $\varepsilon_{r,m}$ is the maximum of ε_r, γ ($\gamma = 1$ for classical ferroelectrics and $\gamma = 2$ for ideal relaxors) and σ represents the relaxor degree. As shown in Fig. S8 and Fig. 3(f), when x increases from 0 to 0.04, γ increases from 1.36 to 1.63 and σ from 25.54 to 85.48, demonstrating that high-entropy doping at the A site significantly enhances the relaxor behavior of phase transition. Finally, benefiting from the denser microstructure, the 0.03-PLSB/0.5-ZSO film exhibits lower dielectric loss, enabling the improvement of E_b and stable energy storage performance.

Fig. 4(a) shows the RT P–E loops of PZO and x-PLSB/0.5-ZSO films near their respective E_b. All the films exhibit typical AFE double hysteresis loops, which gradually become slimmer with the introduction of Sn^{4+} and the increase of x, resulting in obviously decreased P_r and ΔE ($\Delta E = E_F - E_A$). Moreover, as summarized in Fig. 4(b), E_F, E_A and E_b are significantly enhanced by A-site doping, contributing to the increase of P_{max} and ΔP. The 0.03-PLSB/0.5-ZSO film, possessing a high E_b of 3.3 MV cm^{-1}, a large ΔP of 88.6 μC cm^{-2} and a low ΔE of 0.14 MV cm^{-1}, exhibits both a large W_{rec} of 101.8 J cm^{-3} and an η of 71.5%, approximately 3.6 and 2 times higher than those of the pure PZO film ($W_{rec} \sim 28.3$ J cm^{-3} and $\eta \sim 37.6\%$) (Fig. 4(c)), respectively. Fig. 4(d) shows a comparison of W_{rec} and η between our 0.03-PLSB/0.5-ZSO film and recently reported PZO-based films.[10–20,22,23,28,30,32,34,35,42] Notably, the 0.03-PLSB/0.5-ZSO film demonstrates highly competitive W_{rec} and η, making it a promising dielectric material for energy storage application.

3.3. Mechanism of the enhanced energy storage properties

To understand the superior energy storage performance of the 0.03-PLSB/0.5-ZSO film, its leakage current density (J) and microstructure are investigated. As shown by the J-E curves in Fig. 5(a), compared with PZO, the J values of x-PLSB/0.5-ZSO films not only decrease by 1–2 orders of magnitude but also show different field-dependent behavior. Pb volatilization at high temperature causes the formation of lead vacancies (V_{Pb}^{2-}) and oxygen vacancies (V_O^{2+}):

$$Pb^{2+} + O^{2-} \leftrightarrow PbO\uparrow + V_{Pb}^{2-} + V_O^{2+} \quad (7)$$

These charged defects provide pathways for carrier migration and thus contribute to the leakage current.[43] XPS spectra in Fig. 5(b) show that, in addition to the main peak near 529.8 eV corresponding to lattice oxygen, the O 1s spectra exhibit distinct shoulders at higher binding energies. Based on the Gaussian–Lorentzian fitting, all the O 1s spectra can be divided

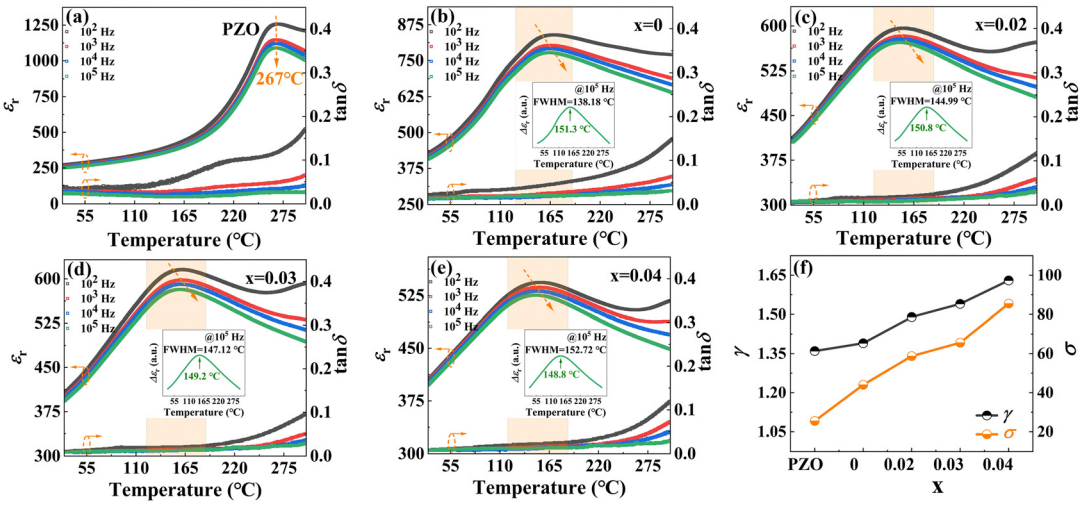

Fig. 3 (a)–(e) Temperature-dependent dielectric constant (ε_r) and loss (tan δ) of PZO and x-PLSB/0.5-ZSO films, with the insets showing temperature-dependent ε_r measured at 10^5 Hz after subtracting the leakage conduction background. (f) The fitted relaxation factors γ and σ.

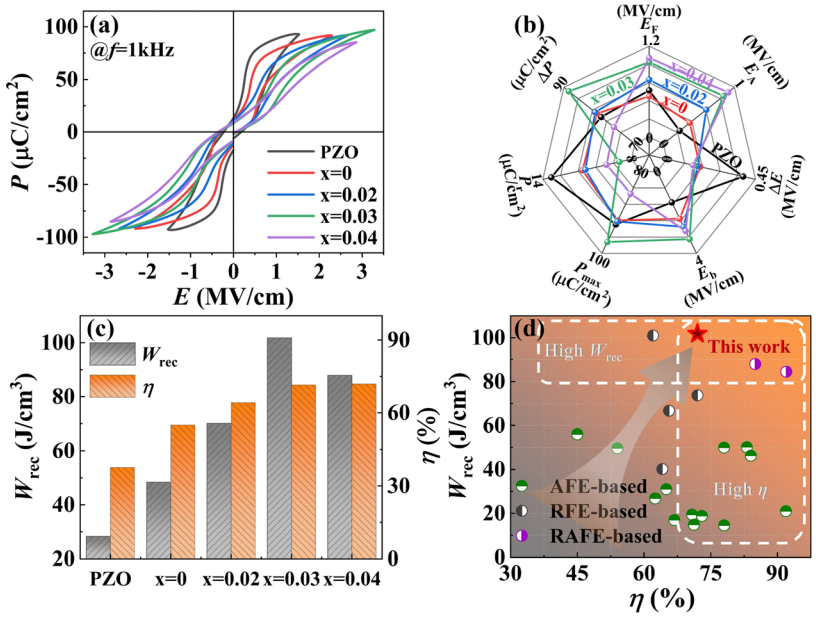

Fig. 4 (a) P–E loops measured near E_b, (b) energy storage parameters, and (c) W_{rec} and η of PZO and x-PLSB/0.5-ZSO films. (d) A comparison of W_{rec} and η between the 0.03-PLSB/0.5-ZSO film and the reported PZO-based films.

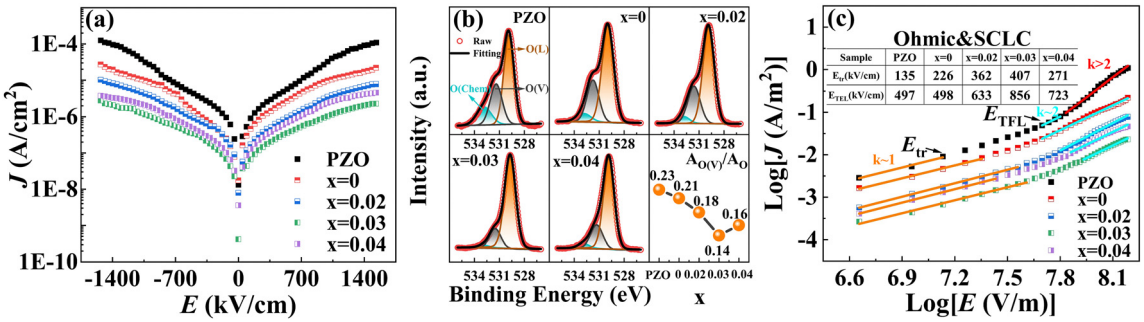

Fig. 5 (a) J–E curves, (b) O 1s XPS spectra, and (c) fitting results of J based on Ohmic and SCLC conduction mechanisms for PZO and x-PLSB/0.5-ZSO films.

into three peaks located at about 529.8 eV, 531.4 eV, and 532.9 eV, corresponding to lattice oxygen (O(L)), V_O^{2+}-related adsorbed oxygen (O(V)), and chemisorbed oxygen (O(Chem)), respectively.[44] The relative concentration of V_O^{2+} can be estimated by $A_{O(V)}/A_O$ (A_O represents the total area of the O 1s peak). With the increase of x, the concentration of V_O^{2+} first decreases and then increases, reaching a minimum at $x = 0.03$ (Fig. 5(b)), which is attributed to the dense microstructure and the suppressed Pb volatilization induced by A-site doping. In contrast, the 0.04-PLSB/0.5-ZSO film possesses more V_O^{2+} than the film with $x = 0.03$ due to its uniform size and thus a relatively loose structure, but less V_O^{2+} than the pure PZO film due to its smaller grains (Fig. S7).

Fig. 5(c) shows the log(J)–log(E) curves of all the films. The orange and cyan lines represent the Ohmic conduction ($J = \sigma E$, slope $k \approx 1$), and the space-charge-limited conduction (SCLC, $J = 9\mu\varepsilon_0\varepsilon_r E^2/8d$, slope $k \approx 2$), respectively.[45] The transition field (E_{tr}) marks the end of pure Ohmic conduction, while the trap-filled limit field (E_{TFL}) marks the onset of single SCLC.[46] As shown in Fig. 5(c) and Fig. S9, with increasing electric field, the conduction mechanism of PZO transitions from Ohmic and SCLC to Schottky emission ($E > 0.68$ MV cm^{-1}). In contrast, the x-PLSB/0.5-ZSO films maintain the SCLC mechanism even at the maximum applied field of 1.53 MV cm^{-1}. Furthermore, owing to the obviously decreased V_{Pb}^{2-} and V_O^{2+}, the 0.03-PLSB/0.5-ZSO film possesses the highest E_{tr} and E_{TFL}, ensuring its enhanced stability at high field. Taken together, the 0.03-PLSB/0.5-ZSO film, benefiting from the least charge defects, an optimal microstructure, and thus a stable conduction mechanism, exhibits the lowest J and the highest E_b.

A relatively large grain was selected for HR-TEM measurement. Fig. 6(a)–(d) show the cross-sectional HR-TEM images of the 0.03-PLSB/0.5-ZSO film along [$\bar{1}$10] and [001] pseudocubic zone axes, together with their corresponding selected-area electron diffraction (SAED) patterns, where the A- and B-site cations are highlighted by yellow and purple circles,

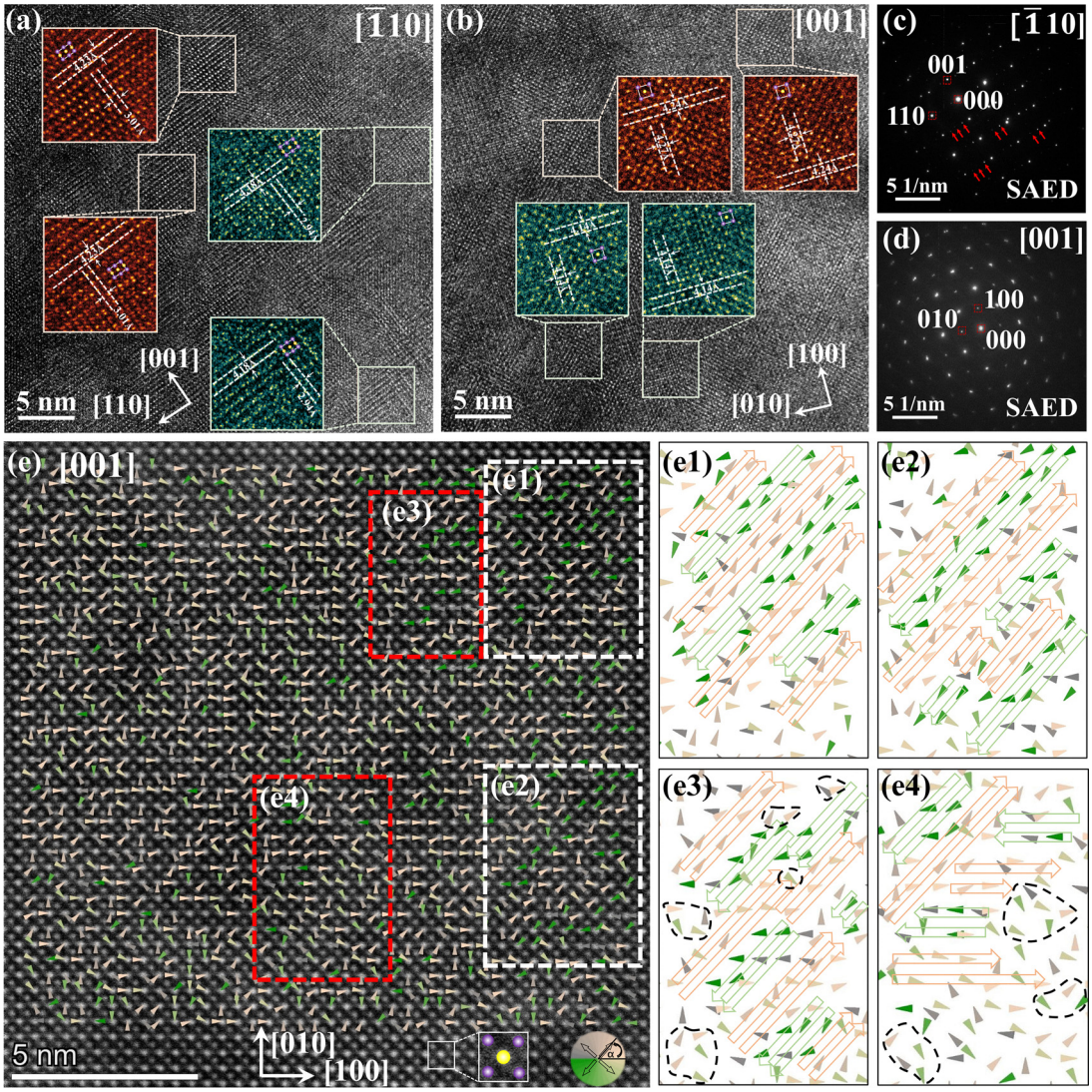

Fig. 6 The cross-sectional HR-TEM images of the 0.03-PLSB/0.5-ZSO film along (a) [1̄10] and (b) [001] zone axes, with corresponding SAED patterns in (c) and (d). (e) Cross-sectional AC-HAADF-STEM image along the [001] zone axis, with magnified views in (e1)–(e4).

respectively. In Fig. 6(a) and (b), regions with well-defined lattice stripes are randomly selected for magnified analysis, and interplanar spacings (d-spacings) are measured using Gatan Microscopy Suite software. The red regions, with d-spacings of 4.24, 4.27 and 4.23 Å for the (100), (010) and (001) crystal planes, respectively, correspond to the AFE_O phase, while the green regions with smaller d-spacings [(100):4.14 Å, (010):4.14 Å, (001):4.18 Å] correspond to the AFE_T phase, directly confirming the coexistence of AFE_O and AFE_T phases. Additionally, the red-arrow-marked points in Fig. 6(c) correspond to the satellite peaks along the (110) direction of the AFE_O phase, indicating a non-ideal fourfold modulation and thus the interruption of the long-range AFE order.

Fig. 6(e) shows the atomic-resolution polarization mapping along the [001] zone axis of the 0.03-PLSB/0.5-ZSO film. The polarization vectors are calculated from the displacement of A-site cations relative to the average position of their four nearest B-site neighbors. Atomic column positions are precisely determined using two-dimensional Gaussian fitting. Polarization mapping in Fig. 6(e), where arrows represent the polarization direction relative to the [100] zone axis, reveals three notable features: (1) all the domains possess nanoscale size, no matter the AFE_O or AFE_T phase. (2) Local polarization vectors exhibit short-range AFE order with ↑↑↓↓ four-period antiparallel arrangements (Fig. 6(e1)–(e4)). (3) In some smaller regions (Fig. 6(e3) and (e4), black dashed boxes), polarization directions are strongly perturbed due to the randomly distributed A- and B-site ions, indicating the pronounced lattice disorder and the polar clusters with sizes of several units. Overall, the coexistence and random distribution of AFE_O and AFE_T phases, together with multielement-induced local lattice disorder, refine the domain size and lower the polarization-switching barrier, thereby reducing ΔE and P_r. As reported by Du *et al.*,[47,48] PFM measurement can further confirm these variations. As shown in Fig. S10, after poling under 12 V, compared with the pure PZO film, the domains of the 0.03-PLSB/0.5-ZSO film relax faster due to its refined domain size and almost return to the

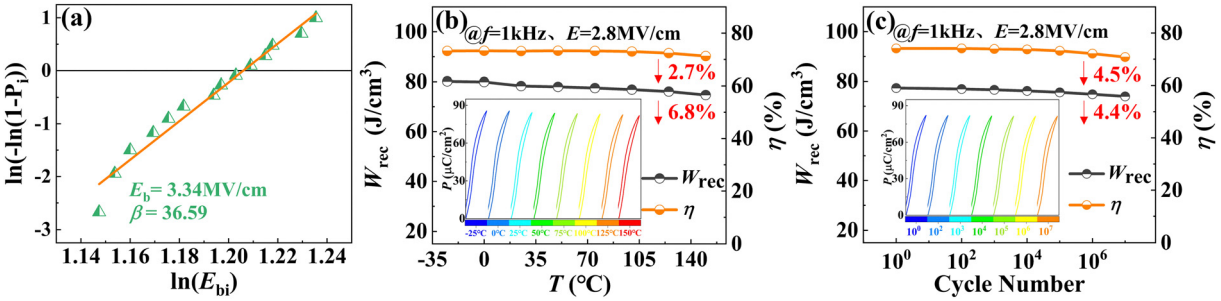

Fig. 7 (a) Weibull distribution of E_b, (b) temperature dependence of W_{rec} and η, and (c) fatigue performance of the 0.03-PLSB/0.5-ZSO film. The insets in (b) and (c) show the P–E loops measured at various temperatures and after various cycle numbers, respectively.

original state after 3 min, being responsible for its decreased ΔE and P_r.

The above features also show a great effect on the electromechanical response. Though AFEs do not exhibit an intrinsic piezoelectric response in their ground state, they can display a pronounced electromechanical response because of the field-induced AFE–FE phase transition.[49] For the 0.03-PLSB/0.5-ZSO film, the coexistence of AFE_O and AFE_T phases facilitates the polarization switching and increases the structural instability, resulting in the largest deformation (Fig. S11). Such an electromechanical response is usually estimated by the effective piezoelectric coefficient,[50] which corresponds to the deformation from the AFE–FE phase transition but not from the inverse piezoelectric effect. As a result, the 0.03-PLSB/0.5-ZSO film exhibits the highest effective piezoelectric coefficient of $\sim$253 pm V^{-1} and optimal energy storage performance, enabling its potential applications in integrated micro-/nano-actuators, sensors and energy storage devices.

3.4. Reliability and stability

The uniformity and reproducibility of the samples can be evaluated using the two-parameter Weibull distribution of E_b:[51]

$$X_i = \ln(E_{bi}) \quad (8)$$

$$P_i = \frac{i}{n+1} \quad (9)$$

$$Y_i = \ln(-\ln(1 - P_i)) \quad (10)$$

where n is the total number of samples, which equals 14 in our experiments, and E_{bi} and P_i represent the E_b and cumulative failure probability of the i-th sample, respectively. Generally, a large fitting parameter β (>10) indicates a narrow distribution of E_b and good uniformity. As shown in Fig. 7(a) and Fig. S12, β of all the films are larger than 17. The statistical E_b is 3.34 MV cm^{-1} for the 0.03-PLSB/0.5-ZSO film, 2.2 times higher than that of pure PZO (1.52 MV cm^{-1}). The enhanced E_b of the 0.03-PLSB/0.5-ZSO film is primarily attributed to the aforementioned lowest concentration of V_O^{2+} and a dense microstructure. Meanwhile, the S_{config} increases from 0.69R for the film with x = 0 to 1.00R, 1.11R and 1.21R for the films with x = 0.02, 0.03 and 0.04, respectively, which amplifies the lattice disorder and thus enhances the electron scattering and further increases E_b. However, excessive A-site doping increases the defect concentration (Fig. 4(b)), leading to a decrease in E_b and W_{rec} of the film with x = 0.04.

Fig. 7(b) shows the P–E loops and the corresponding W_{rec} and η values of the 0.03-PLSB/0.5-ZSO film measured under 2.8 MV cm^{-1} (about 80% of E_b) and in the temperature range from −25 to 150 °C, covering a 175 °C span around RT. W_{rec} and η decrease slightly with increasing temperature, by about 6.8% and 2.7%, respectively. This excellent thermal stability mainly originates from the relaxor phase transition. On the one hand, the dielectric constant varies gently with temperature over a wide range, improving the stability of the polarization and thereby W_{rec}. On the other hand, the polar nano regions (PNRs) and the coexistence of AFE_O and AFE_T phases in the RAFE 0.03-PLSB/0.5-ZSO film (Fig. 6) can induce disordered lattice distortions and thus enhance the electron scattering, suppressing the thermal activation of carriers and stabilizing η.

Fig. 7(c) shows the fatigue endurance of the 0.03-PLSB/0.5-ZSO film under 2.8 MV cm^{-1}. After 10^7 cycles, W_{rec} and η decrease by only 4.4% and 4.5%, respectively, demonstrating excellent fatigue resistance. The fatigue behavior of PZO-based films is generally associated with the domain-wall pinning during polarization switching.[52] In the 0.03-PLSB/0.5-ZSO film, the reduced V_{Pb}^{2-} and V_O^{2+} weaken the domain-wall pinning and thus enhance the reversibility of AFE–FE transition.

Conclusions

In summary, we investigate the energy storage performance of RAFE x-PLSB/y-ZSO thin films, which are designed *via* phase regulation and entropy engineering. B-site Sn^{4+} ions effectively induce the coexistence of AFE_O and AFE_T phases, facilitating polarization switching from the FE phase back to the AFE phase and contributing to the decrease of P_r and ΔE. A-site high-entropy doping with La^{3+}, Sr^{2+} and Ba^{2+} decreases the tolerance factor t and thus increases E_F from the AFE phase to FE phase. Moreover, the random distribution of doping ions suppresses the grain and domain growth and reduces the concentration of V_{Pb}^{2-} and V_O^{2+}, enabling the increase of E_b and a further decrease of P_r and ΔE. Benefiting from these synergistic effects, the 0.03-PLSB/0.5-ZSO film demonstrates enhanced phase-transition

relaxor behavior, an improved E_b (3.34 MV cm^{-1}) and a stable AFE-phase, resulting in a synchronously improved W_{rec} of 101.8 J cm^{-3} and an η of 71.5%. Meanwhile, the film also exhibits superior thermal stability and fatigue endurance. As temperature increases from −25 to 150 °C, the degradation is 6.8% and 2.7%, respectively, for W_{rec} and η. After 10^7 cycles, the variations of W_{rec} and η are both less than 5%. This work offers valuable guidance for improving the comprehensive energy storage performance of AFEs.

Author contributions

Jiaqi Lian: data curation; investigation, writing – original draft; and writing – review and editing. Fengzhen Huang: conceptualization; data curation; formal analysis; funding acquisition; methodology; supervision; and writing – review and editing. Biwei Shen: investigation. Yulong Yang: investigation. Jielin Zha: investigation. Zeyu Xiao: investigation. Kai Cao: investigation. Xiaomei Lu: conceptualization; formal analysis; funding acquisition; methodology; supervision; and writing – review and editing. Jinsong Zhu: formal analysis.

Conflicts of interest

The authors have no conflicts to disclose.

Data availability

The data that support the findings of this study are available within the article and supplementary information (SI). Supplementary information: the schematic illustrations of linear dielectric, ferroelectric and antiferroelectric; *P*–*E* loops, XRD patterns, and temperature-dependent dielectric spectra of the 0.02-PLSB/*y*-ZSO and 0.03-PLSB/*y*-ZSO films; EDS mapping, cross-sectional SEM images, and AFM surface morphologies; fitting of relaxation factors and conduction mechanisms; and time evolution of out-of-plane PFM images, the piezoelectric phase and amplitude, and Weibull distribution of E_b.[53–55] See DOI: https://doi.org/10.1039/d5tc04503g.

Acknowledgements

This work was supported by the Ministry of Science and Technology of China (No. 2022YFA1402903 and 2025YFF05 20301), the National Natural Science Foundation of China (No. 62171214, 52172116 and 12574097), and the Priority Academic Program Development of Jiangsu Higher Education Institutions (PAPD).

References

1 X. K. Wei, N. Domingo, Y. Sun, N. Balke, R. E. Dunin-Borkowski and J. Mayer, *Adv. Energy Mater.*, 2022, **12**, 2201199.
2 K. Aryana, J. A. Tomko, R. Gao, E. R. Hoglund, T. Mimura, S. Makarem, A. Salanova, M. S. B. Hoque, T. W. Pfeifer, D. H. Olson, J. L. Braun, J. Nag, J. C. Read, J. M. Howe, E. J. Opila, L. W. Martin, J. F. Ihlefeld and P. E. Hopkins, *Nat. Commun.*, 2022, **13**, 1573.
3 C. A. Randall, Z. M. Fan, I. Reaney, L. Q. Chen and S. Trolier-Mckinstry, *J. Am. Ceram. Soc.*, 2021, **104**, 3775–3810.
4 H. Pan, A. Kursumovic, Y. H. Lin, C. W. Nan and J. L. Macmanus-Driscoll, *Nanoscale*, 2020, **12**, 19582–19591.
5 W. J. Bi, L. M. Li, G. Tian, J. G. Hao, X. Zhai, H. R. Bai, J. Du, C. Chen, W. Li and L. M. Zheng, *Chem. Eng. J.*, 2023, **478**, 147383.
6 C. Kittel, *Phys. Rev.*, 1951, **82**, 729–732.
7 B. Xu, O. Hellman and L. Bellaiche, *Phys. Rev. B*, 2019, **100**, 020102.
8 Y. Y. Si, T. F. Zhang, C. H. Liu, S. Das, B. Xu, R. G. Burkovsky, X. K. Wei and Z. H. Chen, *Prog. Mater. Sci.*, 2024, **142**, 101231.
9 C. Yin, T. D. Zhang, C. H. Zhang, C. K. Jeong, G. T. Hwang and Q. Chi, *J. Mater. Chem. C*, 2023, **11**, 17003–17011.
10 D. X. Li, X. Y. Meng, F. Peng, Z. H. Yao, Q. H. Guo, M. H. Cao, H. X. Liu and H. Hao, *Ceram. Int.*, 2024, **50**, 51762–51769.
11 D. X. Li, X. Y. Meng, E. H. Zhou, X. X. Chen, Z. H. Shen, Q. H. Guo, Z. H. Yao, M. H. Cao, J. S. Wu, S. J. Zhang, H. X. Liu and H. Hao, *Adv. Funct. Mater.*, 2023, **33**, 2302995.
12 X. H. Hao, J. W. Zhai and X. Yao, *J. Am. Ceram. Soc.*, 2009, **92**, 1133–1135.
13 Q. Q. Chen, Y. Y. Zhang, J. Zhang, H. Shen, R. J. Qi, X. F. Chen, Z. Q. Fu, G. S. Wang, J. Yang, W. Bai and X. D. Tang, *Mater. Sci. Eng. B*, 2022, **286**, 116024.
14 Y. Z. Li, Z. J. Wang, Y. Bai and Z. D. Zhang, *J. Eur. Ceram. Soc.*, 2020, **40**, 1285–1292.
15 B. L. Peng, Q. Zhang, X. Li, T. Y. Sun, H. Q. Fan, S. M. Ke, M. Ye, Y. Wang, W. Lu, H. B. Niu, X. R. Zeng and H. T. Huang, *ACS Appl. Mater. Interfaces*, 2015, **7**, 13512–13517.
16 C. W. Ahn, G. Amarsanaa, S. S. Won, S. A. Chae, D. S. Lee and W. Kim, *ACS Appl. Mater. Interfaces*, 2015, **7**, 26381–26386.
17 C. Liu, S. X. Lin, M. H. Qin, X. B. Lu, X. S. Gao, M. Zeng, Q. L. Li and J. M. Liu, *Appl. Phys. Lett.*, 2016, **108**, 112903.
18 X. Guo, J. Ge, F. Ponchel, D. Rémiens, Y. Chen, X. L. Dong and G. S. Wang, *Thin Solid Films*, 2017, **632**, 93–96.
19 M. Ye, Q. Sun, X. Q. Chen, Z. H. Jiang and F. P. Wang, *J. Am. Ceram. Soc.*, 2011, **94**, 3234–3236.
20 Z. Lin, Y. Chen, Z. Liu, G. S. Wang, D. Rémiens and X. L. Dong, *J. Eur. Ceram. Soc.*, 2018, **38**, 3177–3181.
21 Y. Y. Si, T. F. Zhang, Z. H. Chen, Q. H. Zhang, S. Xu, T. Lin, H. L. Huang, C. Zhou, S. Q. Chen, S. Z. Liu, Y. Q. Dong, C. H. Liu, Y. L. Tang, Y. L. Lu, K. J. Jin, E. J. Guo and X. Lin, *ACS Appl. Mater. Interfaces*, 2022, **14**, 51096–51104.
22 T. F. Zhang, Y. Y. Si, S. Q. Deng, H. L. Wang, T. Wang, J. D. Shao, Y. J. Li, X. D. Li, Q. X. Chen, C. H. Liu, G. K. Zhong, Y. Huang, J. Wei, L. Chen, S. Das and Z. H. Chen, *Adv. Funct. Mater.*, 2023, **34**, 2311160.
23 M. D. Nguyen, T. T. Trinh, H. T. Dang and H. N. Vu, *Thin Solid Films*, 2020, **697**, 137794.

24 H. Pan, Z. S. Tian, M. Acharya, X. X. Huang, P. Kavle, H. R. Zhang, L. Y. Wu, D. F. Chen, J. Carroll, R. Scales, C. J. G. Meyers, K. Coleman, B. Hanrahan, J. E. Spanier and L. W. Martin, *Adv. Mater.*, 2023, **35**, 2300257.
25 Y. X. Zhou, T. F. Zhang, L. Chen, H. F. Yu, R. Y. Wang, H. Zhang, J. Wu, S. Q. Deng, H. Qi, C. Zhou and J. Chen, *Nat. Commun.*, 2025, **16**, 805.
26 S. M. Wang, J. Q. Lian, M. Xu, F. Z. Huang, Y. L. Yang, J. L. Zha, X. M. Lu and J. S. Zhu, *J. Phys. D: Appl. Phys.*, 2025, **58**, 185303.
27 M. Z. Sun, X. M. Wang, P. Li, J. Du, P. Fu, J. G. Hao, W. Li and J. W. Zhai, *J. Eur. Ceram. Soc.*, 2023, **43**, 974–985.
28 B. W. Shen, F. Z. Huang, L. Lei, Z. J. Wu, X. L. Hu, Z. Q. Xu, L. Liu, Y. Ye and X. M. Lu, *Appl. Phys. Lett.*, 2023, **123**, 072905.
29 Z. H. Liu, Z. X. Guo, H. Y. Wan, Y. Yuan, H. Yang, H. Wu, W. Ren and Z. G. Ye, *J. Mater. Chem. C*, 2022, **10**, 6762–6769.
30 A. H. Zhang, W. Wang, Q. J. Li, J. Y. Zhu, D. D. Wang, X. B. Lu, M. Zeng, L. M. Yao and Z. B. Pan, *Appl. Phys. Lett.*, 2020, **117**, 252901.
31 M. D. Nguyen, Y. A. Birkhölzer, E. P. Houwman, G. Koster and G. Rijnders, *Adv. Energy Mater.*, 2022, **12**, 2200517.
32 Q. Wu, Y. S. Zhao, Y. P. Zhou, X. H. Chen, X. Wu and S. F. Zhao, *J. Alloys Compd.*, 2021, **881**, 160576.
33 B. B. Yang, Y. Q. Liu, R. J. Jiang, S. Lan, S. Z. Liu, Z. F. Zhou, L. Dou, M. Zhang, H. B. Huang, L. Q. Chen, Y. L. Zhu, S. J. Zhang, X. L. Ma, C. W. Nan and Y. H. Lin, *Nature*, 2025, **637**, 1104–1110.
34 Y. Son, S. Udovenko, A. P. S. Gaur, J. Cui, X. L. Tan and S. Trolier-Mckinstry, *Appl. Phys. Lett.*, 2024, **125**, 212905.
35 X. H. Hao, Y. Wang, L. Zhang, L. W. Zhang and S. L. An, *Appl. Phys. Lett.*, 2013, **102**, 163903.
36 T. Lu, A. J. Studer, D. H. Yu, R. L. Withers, Y. J. Feng, H. Chen, S. S. Islam, Z. Xu and Y. Liu, *Phys. Rev. B*, 2017, **96**, 214108.
37 X. W. Wang, F. Yang, K. X. Yu, B. H. Zhang, J. Y. Chen, Y. J. Shi, P. F. Yang, L. F. He, H. N. Li, R. Liu, X. F. Li, Y. C. Hu, J. Shang and S. Q. Yin, *Adv. Mater. Technol.*, 2023, **8**, 2202044.
38 B. B. Yang, Q. H. Zhang, H. B. Huang, H. Pan, W. X. Zhu, F. Q. Meng, S. Lan, Y. Q. Liu, B. Wei, Y. Q. Liu, L. T. Yang, L. Gu, L. Q. Chen, C. W. Nan and Y. H. Lin, *Nat. Energy*, 2023, **8**, 956.
39 D. L. Corker, A. M. Glazer, J. Dec, K. Roleder and R. W. Whatmore, *Acta Crystallogr., Sect. B*, 1997, **53**, 135–142.
40 Y. P. Liu, T. Y. Hu, M. Liu, R. Lu, L. Lu, Y. Q. Lu, Q. Y. Han, W. J. Fu, T. Z. Duan, Y. Z. Dai, C. R. Ma, S. B. Mi and C. L. Jia, *J. Mater. Chem. A*, 2025, **13**, 4309–4316.
41 P. Mohapatra, Z. M. Fan, J. Cui and X. L. Tan, *J. Eur. Ceram. Soc.*, 2019, **39**, 4735–4742.
42 C. Y. Koo, Y. J. Eum, S. O. Hwang, H. S. Jung, J. H. Yeum, J. Y. Lee and H. Y. Lee, *Ferroelectrics*, 2014, **465**, 89–95.
43 S. Zhang, H. Hao, R. Huang, M. H. Cao, Z. H. Yao and H. X. Liu, *J. Mater. Chem. C*, 2025, **13**, 5555–5564.
44 W. X. Luo, M. X. Wu, Y. F. Han, X. Zhou, L. J. Liu, Q. W. He, P. R. Ren, H. M. Yang, H. Yang, Q. Wang, Z. H. Chen, X. H. Liang and Z. F. Chen, *J. Am. Ceram. Soc.*, 2023, **106**, 4723–4731.
45 L. Shu, X. M. Shi, X. Zhang, Z. Q. Yang, W. Li, Y. P. Ma, Y. X. Liu, L. S. Liu, Y. Y. S. Cheng, L. Y. Wei, Q. Li, H. B. Huang, S. J. Zhang and J. F. Li, *Science*, 2024, **385**, 204–209.
46 F. C. Chiu, *Adv. Mater. Sci. Eng.*, 2014, **2014**, 578168.
47 X. C. Wang, Y. Lu, P. Li, J. Du, P. Fu, J. G. Hao and W. Li, *Inorg. Chem.*, 2024, **63**, 7080–7088.
48 Y. Lu, X. C. Wang, P. Li, J. Du, P. Fu, J. G. Hao and W. Li, *J. Energy Storage*, 2024, **104**, 114508.
49 H. Pan, M. L. Zhu, E. Banyas, L. Alaerts, M. Acharya, H. R. Zhang, J. Kim, X. Z. Chen, X. X. Huang, M. Xu, I. Harris, Z. S. Tian, F. Ricci, B. Hanrahan, J. E. Spanier, G. Hautier, J. M. Lebeau, J. B. Neaton and L. W. Martin, *Nat. Mater.*, 2024, **23**, 944–950.
50 B. C. Lin, K. P. Ong, T. N. Yang, Q. B. Zeng, H. K. Hui, Z. Ye, C. Sim, Z. H. Yen, P. Yang, Y. X. Dou, X. L. Li, X. Y. Gao, C. K. I. Tan, Z. S. Lim, S. W. Zeng, T. Z. Luo, J. L. Xu, X. Tong, P. W. F. Li, M. Q. Ren, K. Y. Zeng, C. L. Sun, S. Ramakrishna, M. B. H. Breese, C. Boothroyd, C. K. Lee, D. J. Singh, Y. M. Lam and H. J. Liu, *Nature*, 2024, **633**, 798–803.
51 L. T. Yang, X. Kong, F. Li, H. Hao, Z. X. Cheng, H. X. Liu, J. F. Li and S. J. Zhang, *Prog. Mater. Sci.*, 2019, **102**, 72–108.
52 Y. Liu, H. Z. Zhang, K. Shapovalov, R. Niu, J. L. M. Cairney, X. Z. Liao, K. Roleder, A. Majchrowski, J. Arbiol, P. Ghosez and G. Catalan, *Nat. Mater.*, 2025, **24**, 1359.
53 D. D. Shangguan, Y. N. Duan, B. L. Wang, C. Wang, J. X. Li, Y. Bai, F. Zhang, Y. Z. Li, Y. S. Wu and Z. J. Wang, *J. Alloys Compd.*, 2021, **870**, 159440.
54 H. Pan, F. Li, Y. Liu, Q. H. Zhang, M. Wang, S. Lan, Y. P. Zheng, J. Ma, L. Gu, Y. Shen, P. Yu, S. J. Zhang, L. Q. Chen, Y. H. Lin and C. W. Nan, *Science*, 2019, **365**, 578–582.
55 E. M. Alkoy and T. Shiosaki, *J. Am. Ceram. Soc.*, 2009, **92**, 396–404.